

Precision measurements of the magnetic parameters of LISA Pathfinder test masses

M Armano,¹ H Audley,² J Baird,³ P Binetruy,^{3,*} M Born,² D Bortoluzzi,⁴ E Castelli,⁵ A Cavalleri,⁶ A Cesarini,⁷ A M Cruise,⁸ K Danzmann,² M de Deus Silva,⁹ I Diepholz,² G Dixon,⁸ R Dolesi,⁵ L Ferraioli,¹⁰ V Ferroni,⁵ E D Fitzsimons,¹¹ M Freschi,⁹ L Gesa,^{12,13,*} D Giardini,¹⁰ F Gibert,^{5,14} R Giusteri,² C Grimani,⁷ J Grzymisch,¹ I Harrison,¹⁵ M-S Hartig,² G Heinzel,² M Hewitson,² D Hollington,¹⁶ D Hoyland,⁸ M Hueller,⁵ H Inchauspé,^{3,17} O Jennrich,¹ P Jetzer,¹⁸ N Karnesis,³ B Kaune,² N Korsakova,¹⁹ C J Killow,²⁰ L Liu,⁵ J A Lobo,^{12,13,*} J P López-Zaragoza,^{12,13,†} R Maarschalkerweerd,¹⁵ D Mance,¹⁰ V Martín,^{12,13} J Martino,³ L Martin-Polo,⁹ F Martin-Portueras,⁹ P W McNamara,¹ J Mendes,¹⁵ L Mendes,⁹ N Meshksar,¹⁰ M Nofrarias,^{12,13,‡} S Paczkowski,² M Perreux-Lloyd,²⁰ A Petiteau,³ P Pivato,⁵ E Plagnol,³ J Ramos-Castro,^{21,13} J Reiche,² F Rivas,^{12,13} D I Robertson,²⁰ G Russano,⁵ D Serrano,^{12,13,§} J Slutsky,²² C F Sopena,^{12,13} T Sumner,¹⁶ D Texier,⁹ J I Thorpe,²² D Vetrugno,⁵ S Vitale,⁵ G Wanner,² H Ward,²⁰ P J Wass,^{16,17} W J Weber,⁵ L Wissel,² A Wittchen,² and P Zweifel¹⁰

¹European Space Technology Centre, European Space Agency, Keplerlaan 1, 2200 AG Noordwijk, The Netherlands

²Albert-Einstein-Institut, Max-Planck-Institut für Gravitationsphysik und Leibniz Universität Hannover, Callinstr. 38, 30167 Hannover, Germany

³APC, Univ Paris Diderot, CNRS/IN2P3, CEA/lrfu, Obs de Paris, Sorbonne Paris Cité, France

⁴Department of Industrial Engineering, University of Trento, via Sommarive 9, 38123 Trento, and Trento Institute for Fundamental Physics and Application / INFN

⁵Dipartimento di Fisica, Università di Trento and Trento Institute for Fundamental Physics and Application / INFN, 38123 Povo, Trento, Italy

⁶Istituto di Fotonica e Nanotecnologie, CNR-Fondazione Bruno Kessler, I-38123 Povo, Trento, Italy

⁷DISPEA, Università di Urbino “Carlo Bo”, Via S. Chiara, 27 61029 Urbino/INFN, Italy

⁸The School of Physics and Astronomy, University of Birmingham, Birmingham, UK

⁹European Space Astronomy Centre, European Space Agency, Villanueva de la Cañada, 28692 Madrid, Spain

¹⁰Institut für Geophysik, ETH Zürich, Sonneggstrasse 5, CH-8092, Zürich, Switzerland

¹¹The UK Astronomy Technology Centre, Royal Observatory, Edinburgh, Blackford Hill, Edinburgh, EH9 3HJ, UK

¹²Institut de Ciències de l’Espai (ICE, CSIC), Campus UAB, Carrer de Can Magrans s/n, 08193 Cerdanyola del Vallès, Spain

¹³Institut d’Estudis Espacials de Catalunya (IEEC), C/ Gran Capità 2-4, 08034 Barcelona, Spain

¹⁴isardSAT SL, Marie Curie 8-14, 08042 Barcelona, Catalonia, Spain

¹⁵European Space Operations Centre, European Space Agency, 64293 Darmstadt, Germany

¹⁶High Energy Physics Group, Physics Department, Imperial College London, Blackett Laboratory, Prince Consort Road, London, SW7 2BW, UK

¹⁷Department of Mechanical and Aerospace Engineering, MAE-A, P.O. Box 116250, University of Florida, Gainesville, Florida 32611, USA

¹⁸Physik Institut, Universität Zürich, Winterthurerstrasse 190, CH-8057 Zürich, Switzerland

¹⁹Observatoire de la Côte d’Azur, Boulevard de l’Observatoire CS 34229 - F 06304 NICE, France

²⁰SUPA, Institute for Gravitational Research, School of Physics and Astronomy, University of Glasgow, Glasgow, G12 8QQ, UK

²¹Department d’Enginyeria Electrònica, Universitat Politècnica de Catalunya, 08034 Barcelona, Spain

²²Gravitational Astrophysics Lab, NASA Goddard Space Flight Center, 8800 Greenbelt Road, Greenbelt, MD 20771 USA

A precise characterization of the magnetic properties of LISA Pathfinder free falling test-masses is of special interest for future gravitational wave observatory in space. Magnetic forces have an important impact on the instrument sensitivity in the low frequency regime below the millihertz. In this paper we report on the magnetic injection experiments performed throughout LISA Pathfinder operations. We show how these experiments allowed a high precision estimate of the instrument magnetic parameters. The remanent magnetic moment was found to have a modulus of $(0.245 \pm 0.081) \text{ nAm}^2$, the x-component of the background magnetic field within the test masses position was measured to be $(414 \pm 74) \text{ nT}$ and its gradient had a value of $(-7.4 \pm 2.1) \mu\text{T/m}$. Finally, we also measured the test mass magnetic susceptibility to be $(-3.35 \pm 0.15) \times 10^{-5}$ in the low frequency regime. All results are in agreement with on-ground estimates.

I. INTRODUCTION

LISA Pathfinder (LPF) [1, 2] was an ESA mission designed as a technology demonstrator for the future gravitational wave observatory in space, LISA [3]. The main goal of the mission was to demonstrate key technologies required to detect gravitational waves in space. In order to do so, the instrument on-board had to achieve a relative acceleration noise between its two

* Deceased

† jplopez@ice.csic.es

‡ nofrarias@ice.csic.es

§ dserrano@ice.csic.es

test masses (TMs) in nominal geodesic motion down to $3 \times 10^{-14} \text{ ms}^{-2} \text{ Hz}^{-1/2}$ at 1 mHz. The relevance of the measurements being its precision in the very low frequency band, a region not achievable with on ground gravitational wave detectors.

LPF launched on December 3rd, 2015 and started its scientific operations on the 1st of March of 2016 after reaching the Lagrange point L1 of the Earth-Sun system. The mission was divided into two different experiments on-board, the European LISA Technology Package (LTP) and the American Disturbance Reduction System (DRS). After seventeen months of scientific operations, the mission successfully demonstrated its main scientific goal, even achieving values of the residual acceleration power spectral density below the LISA requirements along the entire measuring frequency band [4, 20].

Achieving such a demanding level of geodesic free fall was as important as understanding all the different contributions that build the noise model of the instrument. With the goal to design a suitable model for future space-born missions, several experiments were planned during the LPF operations with the scope to split up the noise measurements into its main contributions. With that objective, LISA Pathfinder carried the Data and Diagnostics Subsystem (DDS), which included a temperature measurement subsystem [5, 6], a magnetic diagnostic subsystem [7, 8] and a radiation monitor [9–12].

In this work we will focus on the results of the magnetic diagnostics and, specifically, on the experiments run to characterise the magnetic parameters of the test masses on-board LPF. Getting to know such values more precisely is crucial for the future space-borne gravitational wave observatories, since any magnetic perturbation can have a potential impact on the instrument performance through magnetic parasitic forces.

This work is organised as follows. In section II we describe the magnetic diagnostic system on-board designed to study and disentangle the nature of the magnetic forces, introduced in section III, that can perturb the test mass motion. In section IV we describe the in-flight magnetic experiments performed to extract the TMs magnetic parameters and we present our conclusions in section V.

II. EXPERIMENTAL SETUP

A. The magnetic diagnostics subsystem

The magnetic diagnostics subsystem on-board LISA Pathfinder was in charge of monitoring the magnetic environment and, as well, to induce controlled magnetic fields to perturb the test masses motion in order to properly characterise the contribution of magnetic forces to the total instrument noise budget. To achieve these goals, the subsystem was composed by four tri-axial magnetometers and two induction coils.

The coils —see Fig. 1— were able to inject a controlled

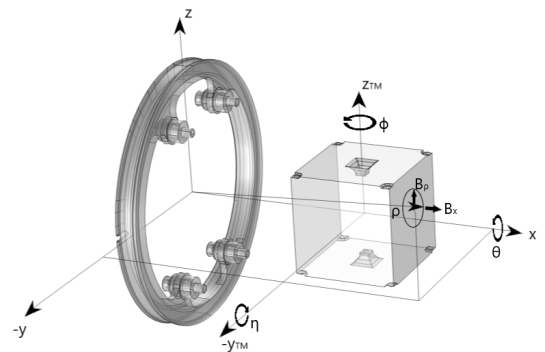


FIG. 1. Coordinate reference system for the coil and the test mass. The convention used for the three angles of rotations along each test mass axis is also shown.

magnetic field within the TMs position as well as in the magnetometers closest to them. Both circular induction coils, with an average radius of 56.5 mm, were located 85.5 mm away from the test masses and they were attached to the external wall of each vacuum enclosure. The wire winding used to build up the coils were made of a Titanium alloy (Ti_6Al_4V) and loop around the structure for a total of 2400 turns. Both coils centres were aligned with the axis, x, joining both TMs centres so that the induced magnetic field had axial symmetry. The four magnetometers were aligned by pairs in each one of the spacecraft axes in order to be able to measure gradients within the spacecraft in both the y and x directions. The entire system was set-up at a same height in the z axis, meaning that no magnetic field gradients along such direction could be measured. Magnetometers were continuously measuring with high precision the evolution of the on-board magnetic field. For each of the measuring axes, each fluxgate magnetometer had a sensing coil surrounding a second inner drive coil around a high permeability magnetic core material. This meaning that all four magnetometers contained active magnetic sensors that had to be located far enough from the test masses for them not to contribute as a source of magnetic parasitic forces.

B. Magnetic environment on-board

The background magnetic field measured on-board was completely dominated by the contribution from the electronics of the spacecraft units. Among them, the thruster systems were a major contributor, both the cold gas high pressure latch valves (the ones used by ESA) and the colloidal thrusters (the ones operated by NASA). Cold gas thrusters or, more precisely, some permanent magnets in the cold gas thruster subsystem, contributed with roughly the 80% of the measured magnetic field. Although a strong contribution, this one remained constant throughout the mission – partially thanks to the high thermal stability reached on-board [6] – which is key for

a mission as LISA with strong requirements on any potential source of fluctuations. This is not the case for the colloidal thrusters, where a persistent slow drift of around 150 nT in the span of 100 days was observed [8]. The main contribution of the magnetic-induced force noise is below the millihertz [13]. In this frequency regime, magnetic field fluctuations are dominated by the interplanetary magnetic field contribution, which can show an important non-stationary component associated with changes in the interplanetary plasma. For instance, variations in the range of 300 – 500 km s⁻¹ in the solar wind velocity were related to variations in the amplitude spectral density in the range 20 – 50 μHz of around 170 – 750 nT Hz^{-1/2} [8].

In what refers to our analysis in the following, we can safely assume that in all the in-flight experiments where we induced magnetic fields with the coils, the background magnetic field (either generated by the spacecraft or due to the interplanetary contribution) can be safely neglected as it was at least one order of magnitude smaller than the ones induced by the coils. The same is true for the gradients of the magnetic fields.

III. MAGNETIC-INDUCED FORCES AND TORQUES IN A FREE FALLING TEST MASS

Magnetic fluctuations can couple into the dynamics of the free falling test masses on-board the satellite. In the following we develop the basic equations needed to describe the experiments carried out with the induction coils in LISA Pathfinder.

A. A magnetic dipole in a surrounding magnetic field

In a first approximation, the free-falling test masses inside LISA Pathfinder can be considered as a magnetic dipole with total magnetic moment density \mathbf{m} inside of a surrounding magnetic field \mathbf{B} . The dipole would therefore feel an associated force and torque given by

$$\mathbf{F} = \langle (\mathbf{m} \cdot \nabla) \mathbf{B} \rangle V, \quad (1a)$$

$$\mathbf{N} = \langle \mathbf{m} \times \mathbf{B} + \mathbf{r} \times (\mathbf{m} \cdot \nabla) \mathbf{B} \rangle V, \quad (1b)$$

where \mathbf{r} denotes the distance to the TM with respect to the coil and we also use the convention $\langle \dots \rangle \equiv \frac{1}{V} \int_V (\dots) d^3x$ to denote TM volume, V , average of the enclosed quantity. In our notation, parameters in bold refer to vectors. The total magnetic moment density \mathbf{m} is the sum of two components: the remanent magnetic moment density \mathbf{m}_r (\mathbf{m} from now on) which depends on the material and manufacturing process and the induced magnetic moment density, \mathbf{m}_i . Given that the dominant material in the test mass composition (73% Au, 27% Pt)

is gold, we assume the magnetic moment to be proportional to the applied magnetic field, i.e.

$$\mathbf{m}_i = \chi / \mu_0 \mathbf{B}, \quad (2)$$

where χ is the magnetic susceptibility. Notice that, although we expect a typical negative susceptibility from a diamagnetic material, we leave the sign undetermined in the following derivation. Also, we have implicitly assumed here an isotropic test mass which allows a scalar susceptibility in the previous equation. Next, we assume the test mass magnetized by a low alternating magnetic field

$$\mathbf{B}(t) = \mathbf{B}^{AC} \sin(\omega t), \quad (3)$$

where \mathbf{B}^{AC} is the amplitude of the oscillating magnetic field and ω the frequency of the applied magnetic field, we will obtain a magnetization that varies with time accordingly, $\mathbf{m}_i(t)$. In diamagnetic, paramagnetic and many ferromagnetic materials, the magnetization also varies sinusoidally and in phase with the applied magnetic field with a constant ratio given by the magnetic susceptibility. However, some ferromagnetic materials show a delayed response that is not in phase with the applied field. This phenomena is typically described by considering the in-phase (χ_r) and out-of-phase (χ_i) components of the magnetic susceptibility. For the case of LPF experiments the most relevant physical mechanism involved in the latter one are Eddy Currents since this contribution becomes increasingly important with the increasing conductivity of the material. However, for most of the experiments at the low frequency regime this component is expected to be orders of magnitude smaller thus, its contribution can be neglected.

Considering both contributions of the magnetization (the remanent and the induced magnetic moments) one can further develop Eqs. (1) into

$$\mathbf{F} = \left\langle (\mathbf{m} \cdot \nabla) \mathbf{B} + \frac{\chi}{\mu_0} [(\mathbf{B} \cdot \nabla) \mathbf{B}] \right\rangle V, \quad (4a)$$

$$\mathbf{N} = \left\langle \mathbf{m} \times \mathbf{B} + \mathbf{r} \times \left[(\mathbf{m} \cdot \nabla) \mathbf{B} + \frac{\chi}{\mu_0} (\mathbf{B} \cdot \nabla) \mathbf{B} \right] \right\rangle V. \quad (4b)$$

In order to describe our experiments in the following sections, we still need to include some more degree of detail in the equations. First, we will consider the magnetic field as composed by an applied, oscillating magnetic field \mathbf{B}^{AC} , and a stable magnetic field \mathbf{B}_0 , divided into an applied time independent DC magnetic field \mathbf{B}^{DC} and some environmental background \mathbf{B}_{back} .

$$\begin{aligned} \mathbf{B} &= \mathbf{B}_0 + \mathbf{B}^{AC} \sin(\omega t) \\ &= (\mathbf{B}_{back} + \mathbf{B}^{DC}) + \mathbf{B}^{AC} \sin(\omega t). \end{aligned} \quad (5)$$

By substituting in Eq. (4a) and factoring out the components in terms of their frequency response to the input signal, we find that the force can be divided into three components: a constant DC term, a term that oscillates at the same frequency of the induced magnetic field 1ω and a term oscillating at twice the frequency 2ω

$$\mathbf{F} = \mathbf{F}_{\text{DC}} + \mathbf{F}_{1\omega} + \mathbf{F}_{2\omega}, \quad (6)$$

with

$$\mathbf{F}_{\text{DC}} = \left[\begin{aligned} &\langle (\mathbf{M} \cdot \nabla) \mathbf{B}_0 \rangle \\ &+ \frac{\chi V}{\mu_0} \left(\langle (\mathbf{B}_0 \cdot \nabla) \mathbf{B}_0 \rangle + \frac{1}{2} \langle (\mathbf{B}^{AC} \cdot \nabla) \mathbf{B}^{AC} \rangle \right) \end{aligned} \right], \quad (7a)$$

$$\mathbf{F}_{1\omega} = \left[\begin{aligned} &\langle (\mathbf{M} \cdot \nabla) \mathbf{B}^{AC} \rangle \\ &+ \frac{\chi V}{\mu_0} \left(\langle (\mathbf{B}_0 \cdot \nabla) \mathbf{B}^{AC} \rangle + \langle (\mathbf{B}^{AC} \cdot \nabla) \mathbf{B}_0 \rangle \right) \end{aligned} \right] \times \sin(\omega t), \quad (7b)$$

$$\mathbf{F}_{2\omega} = \left[-\frac{\chi V}{2\mu_0} \langle (\mathbf{B}^{AC} \cdot \nabla) \mathbf{B}^{AC} \rangle \right] \cos(2\omega t), \quad (7c)$$

where $\mathbf{M} = \mathbf{m}V$ is the remanent magnetic moment and we have assumed homogeneity and stationarity of the test mass properties. Considering that the relative acceleration measurements in LISA Pathfinder are in the x direction, the only component of the force that will be needed is its x component. Analogously, if we manipulate the torque equations a similar result with the three terms before mentioned should appear but that won't be the case as we will see in the next section.

B. Estimate of test mass magnetic parameters

The evaluation of both the force and torque expressions, Eqs. (4a) and (4b) respectively, implies the calculation of the average of an external magnetic field and its gradient within the TMs volume as expressed by $\langle \dots \rangle$. Making use of the induction coils from Figure 1 we can control the injected field ($\mathbf{B}^{AC, DC}$ and $\nabla \mathbf{B}^{AC, DC}$) as it can be calculated by means of Ampère's induction laws under the assumptions of coils with negligible thickness and a wire winding of N turns. Thanks to the symmetry of our system, only the x components of the averaged induced fields are non-zero, $\langle B_x^{AC, DC} \rangle$, and their gradients along the y and z axes can be found to be 3 orders of magnitude smaller than $\langle \nabla_x B_x^{AC, DC} \rangle$ thus, only such

terms will be relevant. Furthermore, the magnetic field in the x direction and its gradient along x can be found to be proportional to one another at any given point in space, that is: $\langle B_x^{AC, DC} \rangle = \kappa \langle \nabla_x B_x^{AC, DC} \rangle$. This factor constant κ only depends on the coil dimensions and the distance from the coil center. Its value can be found analytically for the simple on-axis magnetic field of a coil but it is harder to obtain for the general off-axis magnetic field formula involving elliptic integrals. Thus, its value was calculated numerically to be $\kappa = -0.04487$ m for our particular configuration, with negligible uncertainty originated only due to numerical error. We refer the interested reader to Appendix A for more detail on the calculations involved at the TMs location. Finally, the magnetic force is obtained by applying a heterodyne demodulation at the different frequencies of interest of the on-board measurements of the stray TM force (more detail on this in the upcoming section) resulting in the estimators $\hat{F}_{DC,x}$, $\hat{F}_{1\omega,x}$ and $\hat{F}_{2\omega,x}$. We now proceed to describe how we will estimate the test mass magnetic parameters from the previous generic expressions taking all of that into account.

a. Magnetic susceptibility The coupling between an induced magnetic field and its gradient with the magnetic susceptibility of the test mass is responsible of the appearance of a force component at twice the injected modulation frequency in Eq. (7c). Our analysis can take advantage of this by extracting the signal at 2ω from the measured test mass force, i.e.

$$\chi_{2\omega} = -\frac{2\mu_0}{V} \frac{\hat{F}_{2\omega,x}}{\langle B_x^{AC} \rangle \cdot \langle \nabla_x B_x^{AC} \rangle}, \quad (8)$$

This equation provides a direct estimate of the test mass susceptibility decoupled from any other of the magnetic parameters. The notation in Eq. (8) shows explicitly that the estimate of the susceptibility is obtained at twice the injected frequency by demodulating the encoded information in the Δg and comparing it with the predicted TM average magnetic field and gradient.

We notice that, in principle, we could use the signal at 2ω to obtain both real and imaginary contributions to the magnetic susceptibility. To estimate the imaginary contribution we would need to look for a 2ω contribution with a $\pi/2$ phase shift with respect the original injection. We will explore this in the discussion of our results in Section IV.

b. Remanent magnetic moment The component of the force at the injection frequency, $F_{1\omega,x}$, mixes all the parameters we might be interested in. Taking into advantage that all terms in Eq. (7b) depend on $\langle B_x^{AC} \rangle$ or $\langle \nabla_x B_x^{AC} \rangle$, we can rewrite the expression as follows

$$\hat{F}_{1\omega,x} = \left[M_x + \frac{\chi V}{\mu_0} (B_{0,x} + \kappa \nabla_x B_{0,x}) \right] \langle \nabla_x B_x^{AC} \rangle. \quad (9)$$

The term in brackets can be related to an effective magnetic moment such that

$$M_{eff,x} = M_x + \frac{\chi V}{\mu_0} \left[(B_{back.,x} + \langle B_x^{DC} \rangle) + \kappa \nabla_x (B_{back.,x} + \langle B_x^{DC} \rangle) \right], \quad (10)$$

where we have expanded $B_{0,x}$ as explained in Eq. (5). $B_{back.,x}$ can be considered negligible in front of the injected magnetic field $\langle B_x^{DC} \rangle$ as its value is expected to be an order of magnitude smaller than the injected fields through the coils. Thus, we end up having

$$M_{eff,x} \simeq M_x + \frac{2\chi V}{\mu_0} \langle B_x^{DC} \rangle. \quad (11)$$

If the only variable in Eq. (11) is $\langle B_x^{DC} \rangle$, we will obtain a straight line with an offset that corresponds to the remanent magnetic moment M_x and a slope that is proportional to the magnetic susceptibility χ at 1ω . Furthermore, when we induce a magnetic field in the TM position, using the coils, apart from direct forces in the x direction, we are also generating torques, as described in Eq. (4b). Due to the symmetry of the system the term involving the cross product with \mathbf{r} will integrate to zero across the TM volume due to the alignment between the coil axis and the TMs center resulting in only two components, see Appendix B for the explanation, where only the 1ω term will be of interest leading to the following equations

$$\hat{N}_{\phi,1\omega} = -M_y \langle B_x^{AC} \rangle \quad ; \quad \hat{N}_{\eta,1\omega} = M_z \langle B_x^{AC} \rangle. \quad (12)$$

We can conclude that the 1ω oscillation of the torque in ϕ is directly related to the remanent magnetic moment along y, M_y , while the 1ω oscillation of the torque in η is directly related to the remanent magnetic moment along z, M_z . Therefore, by demodulating the torque at 1ω for η and ϕ and considering the values of the injected magnetic field $\langle B_x^{AC} \rangle$, we will be able to determine M_y and M_z .

c. Background estimates Similarly to the 1ω term, in Eq. (7a), the expression of the DC force component of the signal involves again all the unknown parameters. If we group all the terms of Eq. (7a) as a function of $\langle B_x^{DC} \rangle$, we can rewrite it as:

$$\hat{F}_{DC,x} \simeq \left(\frac{\chi V}{\mu_0 \kappa} \right) \langle B_x^{DC} \rangle^2 + \left[\frac{M_x}{\kappa} + \frac{\chi V}{\mu_0} \left(\nabla_x B_{back.,x} + \frac{B_{back.,x}}{\kappa} \right) \right] \langle B_x^{DC} \rangle +$$

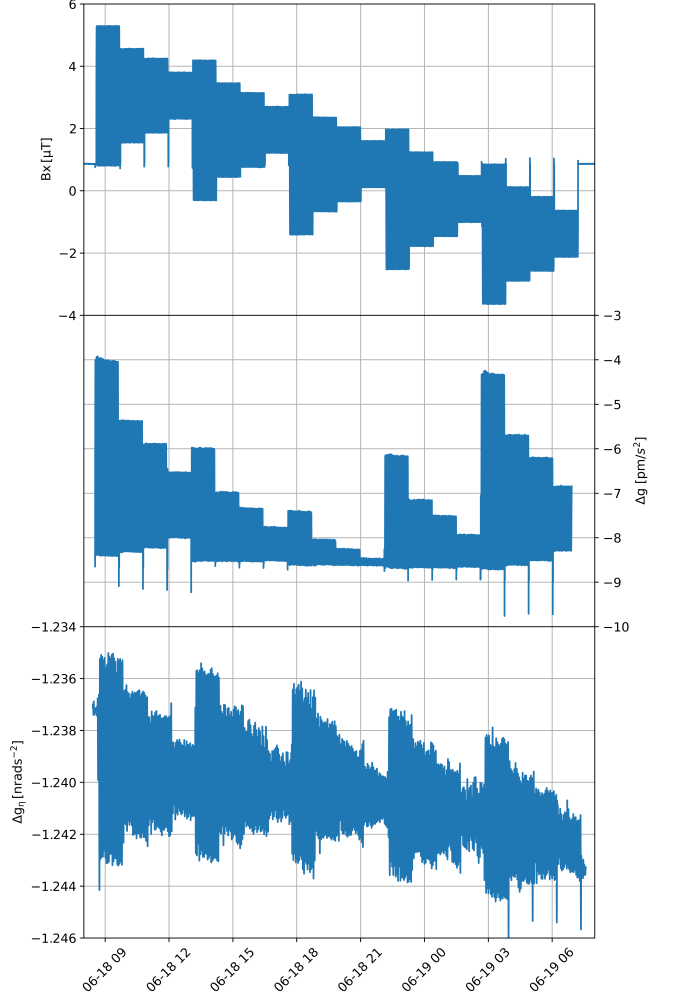


FIG. 2. Experiments with coil #1, June 18th, 2016. *Top*: B_x as measured in the magnetometer closest to the coil, PX. *Middle*: Δg . *Bottom*: Angular acceleration along the rotation angle η .

$$+ \left\{ M_+ \nabla_x B_{back.,x} + \frac{\chi V}{\mu_0} \left[3B_{back.,x} \nabla_x B_{back.,x} + \frac{1}{2} \langle B_x^{AC} \rangle \langle \nabla_x B_x^{AC} \rangle \right] \right\}, \quad (13)$$

where $M_+ = M_x + M_y + M_z$. We have made the assumption that the background magnetic field is the same in all directions, $B_{back.,x} \simeq B_{back.,y} \simeq B_{back.,z}$, because we don't have any information a priori on the magnitude of such variable. We also had to consider that the gradient of $B_{back.,x}$ was the same along all three axes: $\nabla_x B_{back.,x} \simeq \nabla_y B_{back.,x} \simeq \nabla_z B_{back.,x}$, which is a worst case scenario since all components contributing to the background gradient would add up when in reality they could cancel each other. If the only variable is $\langle B_x^{DC} \rangle$, we can observe $\hat{F}_{DC,x}$ follows a quadratic equation.

IV. IN-FLIGHT EXPERIMENTAL CAMPAIGN

Soon after LPF started scientific operations, on March 1st, 2016, magnetic experiments were scheduled to extract the magnetic parameters related to the TMs. The experiments consisted in applying an electric current through the coils to induce a magnetic field in the position of the TMs. The applied current in the coils was a sinusoidal signal $I(t) = I^{DC} + I^{AC} \sin(\omega t)$, where I^{DC} was a constant offset, I^{AC} the amplitude of the sinusoidal signal and ω its angular frequency. The current induces a magnetic field in the surroundings of the coil of the same type $B(t) = B^{DC} + B^{AC} \sin(\omega t)$.

At the beginning of the commissioning period, all subsystems went through an initial checkout procedure. In this initial phase, coil #2—the one closest to TM2—showed a malfunctioning during the verification. Due to this fact, the injections performed during the operations period were on coil #1, and the only set of injections performed in coil #2 were done with low currents to prevent any possible current leak to other systems, which resulted in a reduction of the precision achievable with coil #2 experiments. This implies that most of the results that will be shown here will be for TM1 if not specified otherwise.

We carried a total of three sets of magnetics injections. The first set was injected on the days 28th and 29th of April, 2016. The injection of day 28th consisted on applying a sinusoidal signal through the coil #1 at different DCs and with different AC amplitudes. The injections on day 29th were exactly the same but through coil #2. The second set of injections were carried on the 18th of June, 2016. It consisted on a series of sinusoidal injections at a wider range of both DCs and ACs than the previous ones and exclusively in coil #1. The third, and last, set of injections were performed on the days 14th, 15th and 16th of March, 2017. They consisted on a very long lasting signal at a high DC and with a small sinusoidal on top of it. These were applied exclusively through coil #1 too. The complete list of experiments is shown in Appendix C.

A typical run of magnetic experiments is shown in Figure 2. The three panels display the main variables of interest in our analysis, these are the magnetic field in the x direction, as measured by the closest magnetometer to each coil, the acceleration produced between the TMs due to the presence of these injections and the torque being induced between both TMs along the y axis.

We evaluate the magnetically induced force in the test mass through the Δg variable—the end scientific output of the mission—nominally defined as the differential stray acceleration between the two TMs in their nominal position [20]. Since the main objective of the Δg is the evaluation of the free fall of the test masses, those forces arising in the spacecraft dynamics control loop or others forces originating in the LISA Pathfinder non-inertial reference frame are rightfully subtracted in the definition of this parameter [21]. Indeed, the terms $\hat{F}_{DC,x}$, $\hat{F}_{1\omega,x}$ and $\hat{F}_{2\omega,x}$ previously defined in Section III B are estimated

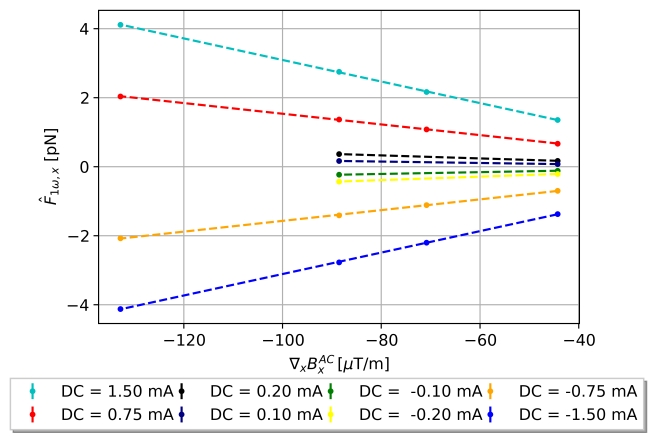


FIG. 3. $\hat{F}_{1\omega,x}$ on TM1 as a function of the applied AC magnetic field gradient. The different colors correspond to fixed DC values of the injected signal.

by demodulating the Δg at the corresponding frequencies and rescaling the amplitudes obtained by means of the mass of the TMs, $m_{\text{TM}} = 1.928$ kg. Analogously, the same procedure can be extrapolated to the torque by using the moment of inertia of a cube with the side length of the TMs, 46 mm.

Since the magnetic field can not be directly measured in the test mass position we must refer to the magnetometers read-out for calibration. Hence, we estimated the amplitude in the PX magnetometer of each of the 20 injections of June 18th, 2016 for coil #1. To do so we demodulate the measured read-out at the injection frequency. By comparing these amplitudes to the ones predicted by Ampère's law we found a systematic discrepancy of $11.85 \pm 0.45\%$ being the predicted magnetic field larger than the measurements from the magnetometers. Magnetometers accuracy of 0.5% allows the most precise calibration to prevent any mechanical tolerances during manufacturing and assembly of the coils and displacements and tilts that may have arisen during launch. In the following, we will apply this correction to all the calculated magnetic field values that intervene in all the equations derived in the previous section and redefine them for simplicity, i.e. $B_x^{AC} \equiv 0.8815 \langle B_x^{AC} \rangle$.

A. Remanent magnetic moment

The estimate of the remanent magnetic moment is obtained through the dependence with the 1ω component of the force expressed in Eq. (9) together with the approximation of Eq. (10), that we recall here for convenience:

$$\hat{F}_{1\omega,x} = \left[M_x + \frac{2\chi V}{\mu_0} B_x^{DC} \right] \nabla_x B_x^{AC}.$$

In order to evaluate this term, during the June 18th run several injections with different AC field gradients were

applied to the TMs. By doing so we can evaluate the term in brackets above at different values of the gradient $\nabla_x B_x^{AC}$. This is shown in Figure 3 where we display how the 1ω component of the force changes depending on the intensity of the injected AC magnetic field gradient, for fixed DCs. Each result in the plot represents an injection at 5 mHz with AC amplitudes applied to the coil of $I^{AC} = 0.5, 0.8, 1.0, 1.5$ mA.

As explained in Section III B, by running the experiment at different DC levels we can further disentangle the dependencies for the parameters inside the brackets and obtain the estimate for the remanent magnetic moment. Table I gathers the linear fits to the results that we also show in Figure 4. The offset parameter corresponds to the remanent magnetic moment of test mass #1 in the x direction, $M_x = 0.140 \pm 0.138$ nAm². The slope parameter is directly related to the magnetic susceptibility at 1ω . However, the values that were used for DCs of $\pm 0.1, 0.2$ mA came from the injections of the 28th of April which were performed at different frequencies, 3 mHz, than the rest at 5 mHz. Thus, to obtain the value of the susceptibility at 5 mHz, we will use the fit from Fig. 4, but with only the DC values of $\pm 0.75, 1.5$ mA giving a result of $\chi_{5\text{mHz}} = (-3.3723 \pm 0.0069) \times 10^{-5}$.

Analogously, to obtain M_y and M_z , we demodulate the amplitudes of the torque measurements around the required angles and apply Eqs. (12) for the respective injected magnetic fields. This way, we obtained $M_y = 0.178 \pm 0.025$ nAm² and $M_z = 0.095 \pm 0.010$ nAm² which we will need for the background estimations. These results lead to a total remanent magnetic moment of: $|\mathbf{M}| = (0.245 \pm 0.081)$ nAm².

B. Background magnetic field

The induction of forces in the test mass by means of the controlled injection of magnetic fields allow the determination not only of the test mass magnetic parameters but also of environment parameters that contribute to the magnetic force, which is the case of the background magnetic field in the test mass position. We emphasize

TABLE I. Coefficients of the fitted lines of Fig. 3 of the type $y = Ax + B$. The errors of the fits for $I^{DC} = \pm 0.1, 0.2$ are 0 because there were only two points to fit the line.

I^{DC} [mA]	A [nAm ²]	B [fN]
1.50	(-31.24 ± 0.25)	(-31 ± 23)
0.75	(-15.48 ± 0.15)	(-13 ± 13)
0.20	(-4.39 ± 0)	(-23 ± 0)
0.10	(-2.04 ± 0)	(-14 ± 0)
-0.10	(2.60 ± 0)	(-1.3 ± 0)
-0.20	(5.00 ± 0)	(13 ± 0)
-0.75	(15.58 ± 0.21)	(-12 ± 19)
-1.50	(31.09 ± 0.23)	(-1.3 ± 21)

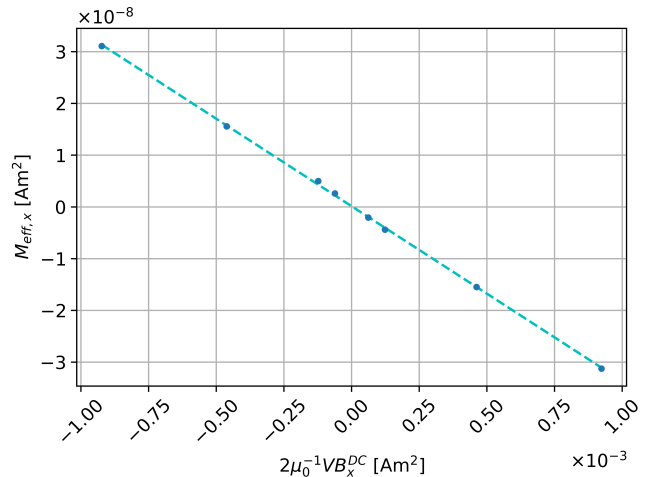


FIG. 4. Effective remanent magnetic moment plotted as a function of the injected DC magnetic field. The result of the fit, for an equation of the type $y = mx + n$, is $m = (-3.380 \pm 0.027) \times 10^{-5}$ and $n = (0.142 \pm 0.140) \times 10^{-9}$ Am².

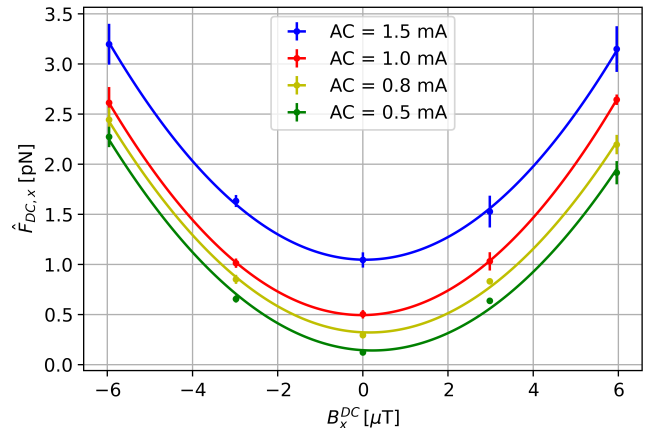


FIG. 5. $\hat{F}_{DC,x}$ on TM1 as a function of the injected DC magnetic field together with their respective fits to an equation of the type $y = Ax^2 + Bx + C$. The different colors correspond to fixed AC values of the injected signal.

here that this is the only precise estimate of this parameter since the magnetometers are located too far away from the test masses to guarantee a precise estimate of this variable.

In order to do so we evaluate Eqs. (13) using the injections of June 18th, 2016. We express the information provided by these runs by displaying the DC component of the measured force as a function of the DC component of the applied magnetic fields. As predicted, we obtain the parabolas in Fig. 5 for different values of the AC amplitude from where we derive the parabola coefficients of Table II.

As derived from Eqs. (13), the A coefficient provides a direct estimate of the magnetic susceptibility

$$A = \left(\frac{\chi V}{\mu_0 \kappa} \right) \quad (14)$$

which, in comparison with other alternative estimates, is not dependent of the injection modulation frequency. The value obtained using equation (14) is $\chi_{DC} = (-3.35 \pm 0.15) \times 10^{-5}$.

With the two remaining terms, B and C, we can build a system of equations, being the two unknowns the parameters that define the background magnetic field in the test mass position, i.e. $B_{back.,x}$ and $\nabla_x B_{back.,x}$

$$C = M_+ \nabla_x B_{back.,x} + \frac{\chi V}{\mu_0} \left[3B_{back.,x} \nabla_x B_{back.,x} + \frac{1}{2} B_x^{AC} \nabla_x B_x^{AC} \right],$$

$$B = \frac{M_x}{\kappa} + \frac{\chi V}{\mu_0} \left[\nabla_x B_{back.,x} + \frac{B_{back.,x}}{\kappa} \right]. \quad (15)$$

Solving this quadratic system of equations, we obtain an expression for the background magnetic field and its gradient in the x direction at the location of the TMs that we can evaluate for each of the four fit values. From the two mathematically available solutions we select the one closer to the estimates of the magnetic field and field gradient obtained during on-ground characterization of the spacecraft, which were 267 nT and -7575 nT/m, respectively [22]. The values that we obtain for the in-flight estimates are $B_{back.,x} = 414 \pm 74$ nT and $\nabla_x B_{back.,x} = -7400 \pm 2100$ nT/m.

C. Magnetic Susceptibility

We have already estimated the test mass magnetic susceptibility as a by product of the estimate of the remanent magnetic moment and the background magnetic field and field gradient.

The DC value of the susceptibility, that is the frequency independent part, was obtained in section IV B and the value of the susceptibility at 5 mHz was measured in section IV A. The rest of the measurements of the

TABLE II. Coefficients of the fitted parabolas of Fig. 5 of the type $y = Ax^2 + Bx + C$.

I^{AC} [mA]	A [N/T ²](10 ⁻²)	B [N/T](10 ⁻⁸)	C [N](10 ⁻¹²)
1.5	(5.99 ± 0.11)	(-0.67 ± 0.39)	(1.047 ± 0.025)
1.0	(6.003 ± 0.025)	(0.265 ± 0.089)	(0.4948 ± 0.0058)
0.8	(5.64 ± 0.16)	(-1.73 ± 0.58)	(0.323 ± 0.038)
0.5	(5.50 ± 0.22)	(-2.46 ± 0.79)	(0.144 ± 0.052)

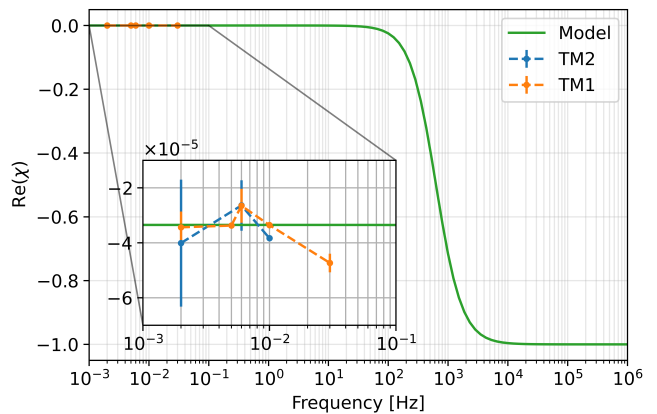


FIG. 6. Magnetic susceptibility of both test masses at different frequencies together with the model predicted by Eq. (16).

magnetic susceptibility of the TMs have been obtained using the 2ω component of the force and Eq. (8). These values correspond to twice the frequency at which the injection was performed. The results of the susceptibilities can be seen in Table III with the value of the frequencies at which they correspond. Using all the injections, from the three different magnetic experiments runs, the frequencies that could be calculated for the magnetic susceptibility were 2, 5, 6, 10 and 30 mHz. In coil #2, for TM2 results, only the injections from the 29th of April were performed, which were at frequencies 1, 3, 5 mHz meaning that only three susceptibility values could be obtained at twice their frequency.

According to [23], the AC magnetic susceptibility of LPF TMs can be approximated at low frequencies as

$$\chi(\omega) \simeq \chi_{DC} + \frac{-i\omega\tau_e}{1 + i\omega\tau_e}, \quad (16)$$

where χ_{DC} is the frequency independent term of the susceptibility and with τ_e being the magnetic susceptibility cut, i.e., the frequency at which the real and imaginary part of the magnetic susceptibility have the same value. For LPF, this value was measured on-ground to be $\tau_e = (2\pi 630)^{-1} \text{Hz}^{-1}$ [24].

TABLE III. Susceptibility values of both TMs obtained at 2ω using Eq. (8) for all the injection frequencies.

Frequency [mHz]	χ_{TM1} (10 ⁻⁵)	χ_{TM2} (10 ⁻⁵)
DC	(-3.35 ± 0.15)	-
2	(-3.43 ± 0.58)	(-4.0 ± 2.3)
5	(-3.3723 ± 0.0069)	-
6	(-2.65 ± 0.62)	(-2.64 ± 0.92)
10	(-3.35 ± 0.12)	(-3.833 ± 0.057)
30	(-4.73 ± 0.34)	-

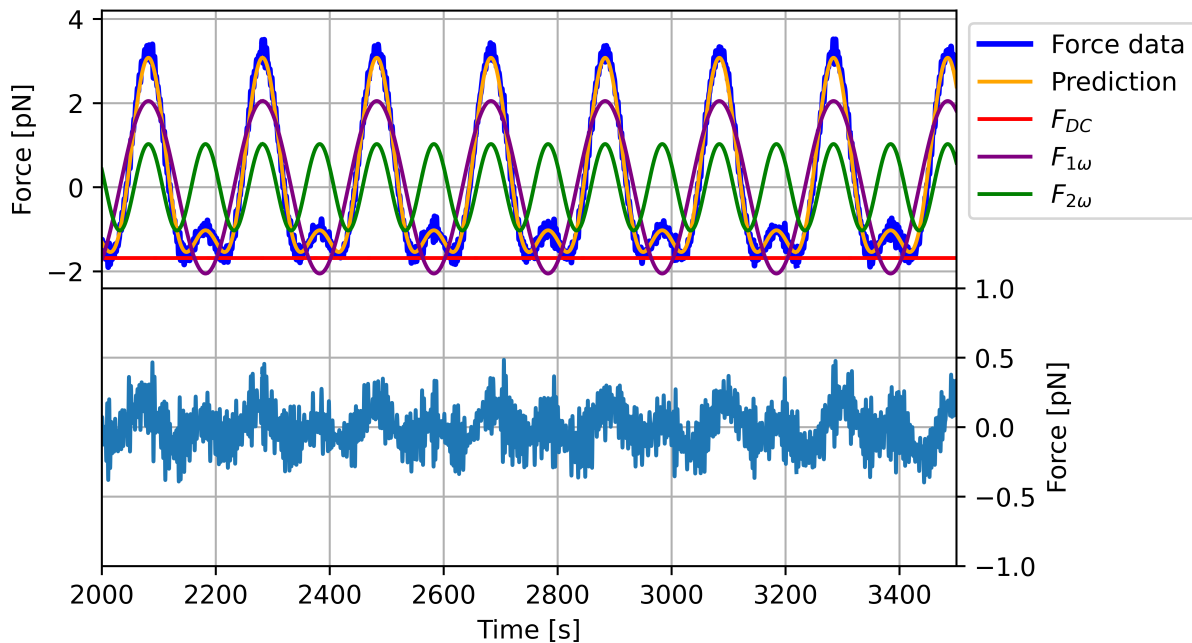


FIG. 7. Detrended force segment of the June injections at $I^{DC} = 0.75$ mA and $I^{AC} = 1.5$ mA compared with the predicted force model together with the three contributions at different frequencies. Below we can see the residual between the measurements and the theoretical prediction.

If we now plot the measured values of the magnetic susceptibility for TMs 1 and 2 along with the curve in Eq. (16), we obtain the plot shown in Figure 6.

The results shown were obtained by heterodyning the Δg signal with a sinusoidal signal in phase. However, if we made the latter be out of phase by $\pi/2$ one would expect the amplitudes measured by this method to be zero only if there was no imaginary component. Thus, the imaginary susceptibility can be obtained demodulating at 2ω , in quadrature. At the frequency regime that we are working on, around the mHz, this value is expected to be orders of magnitude smaller than the real susceptibility. The results that we obtain for the imaginary susceptibility at 10 mHz were consistent with zero, $\chi_i = (0.0 \pm 1.8) \times 10^{-6}$. This is because the method employed to measure the amplitudes of the Δg was limited around the tenths of femtonewtons. So, we can only confirm that the values of the imaginary susceptibility of the TMs are below $|\chi_i| < 1.8 \times 10^{-6}$ at 10 mHz. At the rest of frequencies the result gave a less precise upper bound for the imaginary susceptibility.

Finally, once all parameters are determined, we can evaluate the prediction of our force model in comparison with the measured acceleration during injections. To do so, we have selected a single injection from all the ones of June 18th, 2016 with amplitudes of current DC = 0.75 mA and AC = 1.5 mA. We have used these values for the corresponding magnetic fields DC and AC calcula-

tions respectively together with the magnetic parameters found in the previous sections into Eqs. (7). The results can be seen in Fig. 7 where, together with the total model force, we can also see plotted the different force contributions F_{DC} , $F_{1\omega}$ and $F_{2\omega}$. The predicted force and the data match with a residual difference between them of $(0.0 \pm 1.9) \times 10^{-13}$ N.

V. CONCLUSIONS

The work in this paper presents the most detailed characterisation of the magnetic-induced coupling on free-falling test masses in the context of gravitational wave detection in space. The results and method showed here were originated in the framework of the LISA Pathfinder mission. As a technology demonstrator, LPF represented a unique opportunity for an in-depth description of these effects, which can be directly transferred to LISA and future space-borne gravitational wave detectors.

In our results, we obtain the magnetic parameters defining the response of the free-falling test masses under an external magnetic field. According to these, the test mass remanent magnetic moment do not show any privileged direction, which is in agreement with the hypothesis of an isotropic diamagnetic test mass. We have found the value of its modulus to be: $|\mathbf{M}| = (0.245 \pm 0.081)$ nAm², a result with much better precision than any other on-ground tests and also below the mission requirements of $|\mathbf{M}| \leq 10$ nAm². The background magnetic field,

$B_{back.,x} = 414 \pm 74$ nT, and its gradient, $\nabla_x B_{back.,x} = -7400 \pm 2100$ nT/m, calculated at the location of the TMs are in agreement with the values predicted by [22]. Moreover, the gradient is also below the worst case scenario predicted by [25] which estimated a value of $\nabla_x B_{back.,x} = -11300$ nT/m. The TMs magnetic susceptibility results follow the model predicted by [23] and they are also within the same magnitude when comparing the on-ground estimations for the DC magnetic susceptibility with values around -2.5×10^{-5} [26] with our in-flight DC prediction for the magnetic susceptibility: $\chi_{DC} = (-3.35 \pm 0.15) \times 10^{-5}$. Finally, the value of the imaginary component of the magnetic susceptibility of the TMs has been set to an upper bound at 10 mHz such that: $|\chi_i| < 1.8 \times 10^{-6}$.

These results allow the sound design of future gravitational detectors in space based on results obtained in-flight. They are also key in either reducing or suppressing the need for such a characterisation for future missions, which would otherwise need dedicated time during its commissioning period.

Appendix A: Magnetic field calculation

When the magnetic field is created by an induction coil, such as the case in Fig 1, the laws of Classical Magnetic Theory can be applied to obtain formulas which produce the values of the field and its gradient at any position in space. For slowly varying coil currents and short distances, radiative effects can be neglected.

The system has axial symmetry, hence only parallel (B_x) and transverse (B_ρ) components of the magnetic field are different from zero. Their analytical expressions can be calculated by means of Ampère's induction laws by assuming a coil of negligible thickness and a wire winding of N turns. The result involves elliptic integrals of the first ($K(k)$) and second kind ($E(k)$). This numerical analysis does not take into account mechanical tolerances in the manufacturing and assembly; displacements and tilts induced during launch and in-orbit operations or the implicit calibration of the coil.

1. Elliptic integrals

For the calculation of the average of the magnetic field and its gradient inside the TMs volume we discretized it into 177 parts in all directions, involving the calculations of \mathbf{B} and $\nabla\mathbf{B}$ in a grid of 177^3 points homogeneously distributed. For each point within the grid cell of the TM, the elliptic functions $K(k)$ and $E(k)$ can be evaluated there. The equations to compute are the following, and they should be evaluated in the specified order

$$\rho^2 = y^2 + z^2, \quad (\text{A1})$$

$$k^2 = \frac{4a\rho}{x^2 + (a + \rho)^2}, \quad (\text{A2})$$

$$K(k) = \int_0^{\pi/2} (1 - k^2 \sin^2 \varphi)^{-1/2} d\varphi, \quad (\text{A3})$$

$$E(k) = \int_0^{\pi/2} (1 - k^2 \sin^2 \varphi)^{1/2} d\varphi, \quad (\text{A4})$$

where x, y, z are the cartesian coordinates of the grid cell under calculation w.r.t. the coil center point, a is the coil radius, ρ is the radial distance in cylindrical coordinates and φ is the azimuth angle in cylindrical coordinates.

2. Magnetic field components

The off-axis magnetic field components induced by the coil can be found to be

$$B_\rho(x, \rho) = A_\rho \frac{x}{\rho^{3/2}} F(k), \quad (\text{A5})$$

$$B_x(x, \rho) = A_x \rho^{-3/2} G(k) - \frac{\rho}{x} B_\rho(x, \rho), \quad (\text{A6})$$

where

$$A_\rho = \frac{\mu_0 N I}{4\pi a^{1/2}}, \quad (\text{A7})$$

$$A_x = \frac{a}{2} A_\rho, \quad (\text{A8})$$

$$F(k) = k \left[\frac{1 - k^2/2}{1 - k^2} E(k) - K(k) \right], \quad (\text{A9})$$

$$G(k) = \frac{k^3}{1 - k^2} E(k). \quad (\text{A10})$$

From the latter equations it is easy to derive the components of the magnetic field in their cartesian components

$$B_y = \frac{y}{\rho} B_\rho = \frac{y}{\sqrt{y^2 + z^2}} B_\rho, \quad (\text{A11})$$

$$B_z = \frac{z}{\rho} B_\rho = \frac{z}{\sqrt{y^2 + z^2}} B_\rho. \quad (\text{A12})$$

3. Magnetic field gradient components

Analytical functions for the gradients can also be calculated. Thanks to the symmetry of the system only 5 components out of all 9 possibilities need to be calculated

$$\frac{\partial B_\rho}{\partial x} = A_\rho \rho^{-3/2} \left[F(k) - \frac{x^2}{4a\rho} k^3 \frac{F(k)}{dk} \right], \quad (\text{A13})$$

$$\frac{\partial B_\rho}{\partial \rho} = A_\rho \frac{x}{\rho^{5/2}} \left[-\frac{3}{2} F(k) + \frac{x^2 + a^2 - \rho^2}{8a\rho} k^3 \frac{F(k)}{dk} \right], \quad (\text{A14})$$

$$\frac{\partial B_x}{\partial x} = -A_x \frac{x}{4a\rho^{5/2}} k^3 \frac{G(k)}{dk} - \frac{\rho}{x} \left[\frac{\partial B_\rho}{\partial x} - \frac{1}{x} B_\rho \right], \quad (\text{A15})$$

where

$$\frac{F(k)}{dk} = \frac{1 - k^2 + k^4}{(1 - k^2)^2} E(k) - \frac{1 - k^2/2}{1 - k^2} K(k), \quad (\text{A16})$$

$$\frac{G(k)}{dk} = \frac{k^2}{1 - k^2} \left[\frac{4 - 2k^2}{1 - k^2} E(k) - K(k) \right]. \quad (\text{A17})$$

Finally, we can compute the remaining gradient components by the formulas:

$$\frac{\partial B_y}{\partial x} = \frac{y}{\rho} \frac{\partial B_\rho}{\partial x}, \quad (\text{A18})$$

$$\frac{\partial B_z}{\partial x} = \frac{z}{\rho} \frac{\partial B_\rho}{\partial x}, \quad (\text{A19})$$

$$\frac{\partial B_y}{\partial y} = \frac{y^2}{\rho^2} \frac{\partial B_\rho}{\partial \rho} + \frac{z^2}{\rho^3} B_\rho, \quad (\text{A20})$$

$$\frac{\partial B_y}{\partial z} = \frac{yz}{\rho^2} \left(\frac{\partial B_\rho}{\partial \rho} - \frac{1}{\rho} B_\rho \right). \quad (\text{A21})$$

$$\frac{\partial B_z}{\partial z} = \frac{z^2}{\rho^2} \frac{\partial B_\rho}{\partial \rho} + \frac{y^2}{\rho^3} B_\rho, \quad (\text{A22})$$

The averaged values obtained for a current value of 1 mA are: $\langle B_x \rangle = 4.465 \mu\text{T}$, $\langle B_{y,z} \rangle = 0.327 \text{ fT}$, $\langle \partial B_x / \partial x \rangle = -99.500 \mu\text{T/m}$, $\langle \partial B_x / \partial y, z \rangle = 30.119 \text{ nT/m}$. Hence, the induced field can be considered to only have x components at the TMs for both the magnetic field

and its gradient as the other ones are negligible. Moreover, we note that there is a linear proportionality between $\langle B_x \rangle$ and $\langle \partial B_x / \partial x \rangle$ such that $\langle B_x \rangle = \kappa \langle \partial B_x / \partial x \rangle$. This gives a value $\kappa = -0.04487 \text{ m}$ for the location of the TM with respect to the coil (considering its entire volume) which is independent of the induced current through the coil and only depends on the coil dimensions and the distance to its center point. This constant factor can be determined analytically for the simpler on-axis magnetic field of a coil

$$B_x(x) = \frac{\mu_0 N I a^2}{2(x^2 + a^2)^{3/2}}, \quad (\text{A23})$$

$$\frac{\partial B_x(x)}{\partial x} = -\frac{3\mu_0 N I a^2}{2(x^2 + a^2)^{5/2}} x, \quad (\text{A24})$$

$$\kappa = \frac{B_x}{\partial B_x / \partial x} = -\frac{x^2 + a^2}{3x}, \quad (\text{A25})$$

but is harder when involved with elliptic integrals. Thus, we simply determined its value numerically by considering different currents and distances and we obtained a numerical error many orders of magnitude below: 10^{-16} .

Appendix B: Magnetic torque

From Eq. (4b) we can obtain the torque along the three axis of the TM: θ , η and ϕ . However, LPF interferometric system is not sensitive to rotations around the x axis since it is the one aligned with the laser beam (thus, such given rotations do not affect the distance x between both TMs so we cannot observe them with the Δg). Hence, we will only be able to extract information from the two remaining terms $N_{\eta,\phi}$. Without loss of generality, we will analyze N_η in detail as the same can be done for the other one. For simplicity, assume the induced magnetic field is only composed of an AC term such that $\mathbf{B} = \mathbf{B}^{AC} \sin(\omega t)$, then

$$N_\eta = \langle \sin(\omega t) (m_z B_x^{AC} - m_x B_z^{AC}) \rangle + \langle [r_z \Omega_x - r_x \Omega_z] \rangle, \quad (\text{B1})$$

where

$$\mathbf{\Omega} = (\mathbf{m} \cdot \nabla) \mathbf{B}^{AC} \sin(\omega t) + \frac{\chi}{\mu_0} \left(\frac{1 - \cos(2\omega t)}{2} \right) (\mathbf{B}^{AC} \nabla) \mathbf{B}^{AC}, \quad (\text{B2})$$

we note that the torque can have a component at twice the injected frequency, 2ω . In the previous section we saw that the only non-negligible component of the induced

magnetic field \mathbf{B}^{AC} is in the x direction. Thus, in the first term of Eq. (B1) the component proportional to B_z^{AC} can be removed. Furthermore, we can see that the z component of $\mathbf{\Omega}$, Ω_z , depends on B_z^{AC} meaning that it will equal zero as well. Finally, the element that depends on r_z cannot be cancelled so easily but note that we are integrating over the TM volume meaning that r_z will take opposite signs due to the symmetry of the system thus, averaging to zero. The same will be true for r_y (but not for r_x , this component disappears thanks to Ω_z). We are left with

$$N_\eta = \langle m_z B_x^{AC} \rangle \sin(\omega t). \quad (\text{B3})$$

The same can be done for N_ϕ

$$N_\phi = \langle -m_y B_x^{AC} \rangle \sin(\omega t). \quad (\text{B4})$$

This derivation also holds true if the induced magnetic field includes some background or DC components. This will result on the torque being composed of both a DC term and another one proportional to 1ω

$$\mathbf{N} = \mathbf{N}_{DC} + \mathbf{N}_{1\omega}, \quad (\text{B5})$$

where

$$\mathbf{N}_{DC} = \langle \mathbf{m} \times \mathbf{B}_0 \rangle, \quad (\text{B6a})$$

$$\mathbf{N}_{1\omega} = \langle \mathbf{m} \times \mathbf{B}^{AC} \rangle \sin(\omega t). \quad (\text{B6b})$$

Appendix C: Magnetic experiments

We list here the magnetic experiments during LISA Pathfinder operations together with the parameters used to command the coils on-board.

TABLE IV. 1st set of injections, in coil #1 (April 28th, 2016).

DOY f [mHz]	I_{DC} [mA]	I_{AC} [mA]	duration [s]
119	5	-0.2	1000
119	5	-0.1	1000
119	5	0.00	1000
119	5	+0.1	1000
119	5	+0.2	1000
119	3	-0.2	1000
119	3	-0.1	1000
119	3	0.00	1000
119	3	+0.1	1000
119	3	+0.2	1000
119	1	0.00	20000

TABLE V. 2nd set of injections, in coil #2 (April 29th, 2016).

DOY f [mHz]	I_{DC} [mA]	I_{AC} [mA]	duration [s]
120	5	-0.2	1000
120	5	-0.1	1000
120	5	0.00	1000
120	5	+0.1	1000
120	5	+0.2	1000
120	3	-0.2	1000
120	3	-0.1	1000
120	3	0.00	1000
120	3	+0.1	1000
120	3	+0.2	1000
120	1	0.00	20000

TABLE VI. 3rd set of injections, in coil #1 (June 18th, 2016).

DOY f [mHz]	I_{DC} [mA]	I_{AC} [mA]	duration [s]	
170	5	+1.5	4000	
170	5	+1.5	1.0	4000
170	5	+1.5	0.8	4000
170	5	+1.5	0.5	4000
170	5	+0.75	1.5	4000
170	5	+0.75	1.0	4000
170	5	+0.75	0.8	4000
170	5	+0.75	0.5	4000
170	5	0.00	1.5	4000
170	5	0.00	1.0	4000
170	5	0.00	0.8	4000
170	5	0.00	0.5	4000
170	5	-0.75	1.5	4000
170	5	-0.75	1.0	4000
170	5	-0.75	0.8	4000
170	5	-0.75	0.5	4000
170	5	-1.5	1.5	4000
170	5	-1.5	1.0	4000
170	5	-1.5	0.8	4000
170	5	-1.5	0.5	4000

TABLE VII. Last set of injections, in coil #1 (From March 14th, 2017 to March 16th, 2017).

DOY f [mHz]	I_{DC} [mA]	I_{AC} [mA]	duration [s]	
73	15	-0.5	0.07	75000
74	15	+0.5	0.07	75000
75	15	+1.0	0.07	75000

- [1] S. Anza *et al.*, *Class. Quant. Grav.* **22**, S125 (2005).
- [2] F. Antonucci, M. Armano, H. Audley, G. Auger, M. Benedetti, P. Binetruy, J. Bogenstahl, D. Bortoluzzi, P. Bosetti, N. Brandt, M. Caleno, P. Cañizares, A. Cavalleri, M. Cesa, M. Chmeissani, A. Conchillo, G. Congedo, I. Cristofolini, M. Cruise, K. Danzmann, F. D. Marchi, M. Diaz-Aguilo, I. Diepholz, G. Dixon, R. Dolesi, N. Dunbar, J. Fauste, L. Ferraioli, V. Ferrone, W. Fichter, E. Fitzsimons, M. Freschi, A. G. Marin, C. G. Marirrodriga, R. Gerndt, L. Gesa, F. Gilbert, D. Giardini, C. Grimani, A. Grynagier, B. Guillaume, F. Guzmán, I. Harrison, G. Heinzl, V. Hernández, M. Hewitson, D. Hollington, J. Hough, D. Hoyland, M. Hueller, J. Huesler, O. Jennrich, P. Jetzer, B. Johlander, N. Karnesis, C. Killow, X. Llamas, I. Lloro, A. Lobo, R. Maarschalkerweerd, S. Madden, D. Mance, I. Mateos, P. W. McNamara, J. Mendes, E. Mitchell, A. Monsky, D. Nicolini, D. Nicolodi, M. Nofrarias, F. Pedersen, M. Perreur-Lloyd, E. Plagnol, P. Prat, G. D. Racca, J. Ramos-Castro, J. Reiche, J. A. R. Perez, D. Robertson, H. Rozemeijer, J. Sanjuan, A. Schleicher, M. Schulte, D. Shaul, L. Stagnaro, S. Strandmoe, F. Steier, T. J. Sumner, A. Taylor, D. Texier, C. Trenkel, H.-B. Tu, S. Vitale, G. Wanner, H. Ward, S. Waschke, P. Wass, W. J. Weber, T. Ziegler, and P. Zweifel, *Classical and Quantum Gravity* **29**, 124014 (2012).
- [3] P. Amaro-Seoane, H. Audley, S. Babak, J. Baker, E. Barausse, P. Bender, E. Berti, P. Binetruy, M. Born, D. Bortoluzzi, J. Camp, C. Caprini, V. Cardoso, M. Colpi, J. Conklin, N. Cornish, C. Cutler, K. Danzmann, R. Dolesi, L. Ferraioli, V. Ferroni, E. Fitzsimons, J. Gair, L. Gesa Bote, D. Giardini, F. Gibert, C. Grimani, H. Halloin, G. Heinzl, T. Hertog, M. Hewitson, K. Holley-Bockelmann, D. Hollington, M. Hueller, H. Inchauspe, P. Jetzer, N. Karnesis, C. Killow, A. Klein, B. Klipstein, N. Korsakova, S. L. Larson, J. Livas, I. Lloro, N. Man, D. Mance, J. Martino, I. Mateos, K. McKenzie, S. T. McWilliams, C. Miller, G. Mueller, G. Nardini, G. Nelemans, M. Nofrarias, A. Petiteau, P. Pivato, E. Plagnol, E. Porter, J. Reiche, D. Robertson, N. Robertson, E. Rossi, G. Russano, B. Schutz, A. Sesana, D. Shoemaker, J. Slutsky, C. F. Sopuerta, T. Sumner, N. Tamanini, I. Thorpe, M. Troebis, M. Vallisneri, A. Vecchio, D. Vetrugno, S. Vitale, M. Volonteri, G. Wanner, H. Ward, P. Wass, W. Weber, J. Ziemer, and P. Zweifel, *ArXiv e-prints* (2017).
- [4] M. Armano, H. Audley, J. Baird, P. Binetruy, M. Born, D. Bortoluzzi, E. Castelli, A. Cavalleri, A. Cesarini, A. M. Cruise, K. Danzmann, M. de Deus Silva, I. Diepholz, G. Dixon, R. Dolesi, L. Ferraioli, V. Ferroni, E. D. Fitzsimons, M. Freschi, L. Gesa, F. Gibert, D. Giardini, R. Giusteri, C. Grimani, J. Grzymisch, I. Harrison, G. Heinzl, M. Hewitson, D. Hollington, D. Hoyland, M. Hueller, H. Inchauspe, O. Jennrich, P. Jetzer, N. Karnesis, B. Kaune, N. Korsakova, C. J. Killow, J. A. Lobo, I. Lloro, L. Liu, J. P. López-Zaragoza, R. Maarschalkerweerd, D. Mance, N. Meshksar, V. Martín, L. Martín-Polo, J. Martino, F. Martín-Porqueras, I. Mateos, P. W. McNamara, J. Mendes, L. Mendes, M. Nofrarias, S. Paczkowski, M. Perreur-Lloyd, A. Petiteau, P. Pivato, E. Plagnol, J. Ramos-Castro, J. Reiche, F. Rivas, D. I. Robertson, D. Roma-Dollase, G. Russano, J. Slutsky, C. F. Sopuerta, T. Sumner, D. Telsoni, D. Texier, J. I. Thorpe, C. Trenkel, D. Vetrugno, S. Vitale, G. Wanner, H. Ward, P. J. Wass, D. Wealthy, W. J. Weber, L. Wissel, A. Wittchen, and P. Zweifel, *Monthly Notices of the Royal Astronomical Society* **494**, 3014 (2020), <https://academic.oup.com/mnras/article-pdf/494/2/3014/33129159/staa830.pdf>.
- [5] J. Sanjuán, A. Lobo, M. Nofrarias, J. Ramos-Castro, and P. J. Riu, *Review of Scientific Instruments* **78**, 104904 (2007).
- [6] M. Armano, H. Audley, J. Baird, P. Binetruy, M. Born, D. Bortoluzzi, E. Castelli, A. Cavalleri, A. Cesarini, A. M. Cruise, K. Danzmann, M. de Deus Silva, I. Diepholz, G. Dixon, R. Dolesi, L. Ferraioli, V. Ferroni, E. D. Fitzsimons, M. Freschi, L. Gesa, F. Gibert, D. Giardini, R. Giusteri, C. Grimani, J. Grzymisch, I. Harrison, G. Heinzl, M. Hewitson, D. Hollington, D. Hoyland, M. Hueller, H. Inchauspe, O. Jennrich, P. Jetzer, N. Karnesis, B. Kaune, N. Korsakova, C. J. Killow, J. A. Lobo, I. Lloro, L. Liu, J. P. López-Zaragoza, R. Maarschalkerweerd, D. Mance, C. Mansanet, V. Martín, L. Martín-Polo, J. Martino, F. Martín-Porqueras, I. Mateos, P. W. McNamara, J. Mendes, L. Mendes, N. Meshksar, M. Nofrarias, S. Paczkowski, M. Perreur-Lloyd, A. Petiteau, P. Pivato, E. Plagnol, J. Ramos-Castro, J. Reiche, D. I. Robertson, F. Rivas, G. Russano, J. Sanjuán, J. Slutsky, C. F. Sopuerta, T. Sumner, D. Texier, J. I. Thorpe, C. Trenkel, D. Vetrugno, S. Vitale, G. Wanner, H. Ward, P. J. Wass, D. Wealthy, W. J. Weber, L. Wissel, A. Wittchen, and P. Zweifel, *Monthly Notices of the Royal Astronomical Society* **486**, 3368 (2019), <http://oup.prod.sis.lan/mnras/article-pdf/486/3/3368/28536406/stz1017.pdf>.
- [7] M. Diaz-Aguiló, I. Mateos, J. Ramos-Castro, A. Lobo, and E. García-Berro, *Aerospace Science and Technology* **26**, 53 (2013).
- [8] M. Armano, H. Audley, J. Baird, P. Binetruy, M. Born, D. Bortoluzzi, E. Castelli, A. Cavalleri, A. Cesarini, A. M. Cruise, K. Danzmann, M. de Deus Silva, I. Diepholz, G. Dixon, R. Dolesi, L. Ferraioli, V. Ferroni, E. D. Fitzsimons, M. Freschi, L. Gesa, F. Gibert, D. Giardini, R. Giusteri, C. Grimani, J. Grzymisch, I. Harrison, M.-S. Hartig, G. Heinzl, M. Hewitson, D. Hollington, D. Hoyland, M. Hueller, H. Inchauspe, O. Jennrich, P. Jetzer, N. Karnesis, B. Kaune, N. Korsakova, C. J. Killow, J. A. Lobo, L. Liu, J. P. López-Zaragoza, R. Maarschalkerweerd, D. Mance, V. Martín, L. Martín-Polo, J. Martino, F. Martín-Porqueras, I. Mateos, P. W. McNamara, J. Mendes, L. Mendes, N. Meshksar, M. Nofrarias, S. Paczkowski, M. Perreur-Lloyd, A. Petiteau, P. Pivato, E. Plagnol, J. Ramos-Castro, J. Reiche, F. Rivas, D. I. Robertson, D. Roma-Dollase, G. Russano, J. Slutsky, C. F. Sopuerta, T. Sumner, D. Telsoni, D. Texier, J. I. Thorpe, C. Trenkel, D. Vetrugno, S. Vitale, G. Wanner, H. Ward, P. J. Wass, D. Wealthy, W. J. Weber, L. Wissel, A. Wittchen, and P. Zweifel, *Monthly Notices of the Royal Astronomical Society* **494**, 3014 (2020), <https://academic.oup.com/mnras/article-pdf/494/2/3014/33129159/staa830.pdf>.
- [9] P. Canizares *et al.*, *Class. Quant. Grav.* **26**, 094005 (2009), [arXiv:0810.1491 \[gr-qc\]](https://arxiv.org/abs/0810.1491).
- [10] P. Canizares, M. Chmeissani, A. Conchillo, M. Diaz-Aguiló, E. García-Berro, L. Gesa, F. Gibert, C. Grimani,

- I. Lloro, A. Lobo, I. Mateos, M. Nofrarias, J. Ramos-Castro, J. Sanjuán, C. F. Sopena, H. M. Araújo, and P. Wass, *Classical and Quantum Gravity* **28**, 094004 (2011).
- [11] M. Armano, H. Audley, J. Baird, M. Bassan, S. Benella, P. Binetruy, M. Born, D. Bortoluzzi, A. Cavalleri, A. Cesarini, A. M. Cruise, K. Danzmann, M. de Deus Silva, I. Diepholz, G. Dixon, R. Dolesi, M. Fabi, L. Ferraioli, V. Ferroni, N. Finetti, E. D. Fitzsimons, M. Freschi, L. Gesa, F. Gibert, D. Giardini, R. Giusteri, C. Grimaldi, J. Grzysch, I. Harrison, G. Heinzl, M. Hewitson, D. Hollington, D. Hoyland, M. Hueller, H. Inchauspé, O. Jennrich, P. Jetzer, N. Karnesis, B. Kaune, N. Korsakova, C. J. Killow, M. Laurenza, J. A. Lobo, I. Lloro, L. Liu, J. P. López-Zaragoza, R. Maarschalkerweerd, D. Mance, V. Martín, L. Martin-Polo, J. Martino, F. Martin-Porqueras, S. Madden, I. Mateos, P. W. McNamara, J. Mendes, L. Mendes, A. Monsky, D. Nicolodi, M. Nofrarias, S. Paczkowski, M. Perreur-Lloyd, A. Petiteau, P. Pivato, E. Plagnol, P. Prat, U. Ragnit, B. Raïs, J. Ramos-Castro, J. Reiche, D. I. Robertson, H. Rozemeijer, F. Rivas, G. Russano, J. Sanjuán, P. Sarra, A. Schleicher, D. Shaul, J. Slutsky, C. F. Sopena, R. Stanga, F. Steier, T. Sumner, D. Texier, J. I. Thorpe, C. Trenkel, M. Tröbs, H. B. Tu, D. Vetrugno, S. Vitale, V. Wand, G. Wanner, H. Ward, C. Warren, P. J. Wass, D. Wealthy, W. J. Weber, L. Wissel, A. Wittchen, A. Zambotti, C. Zanon, T. Ziegler, and P. Zweifel, *Phys. Rev. Lett.* **116**, 231101 (2016).
- [21] M. Armano, H. Audley, J. Baird, P. Binetruy, M. Born, D. Bortoluzzi, E. Castelli, A. Cavalleri, A. Cesarini, A. M. Cruise, K. Danzmann, M. de Deus Silva, I. Diepholz, G. Dixon, R. Dolesi, L. Ferraioli, V. Ferroni, E. D. Fitzsimons, M. Freschi, L. Gesa, F. Gibert, D. Giardini, R. Giusteri, C. Grimaldi, J. Grzysch, I. Harrison, G. Heinzl, M. Hewitson, D. Hollington, D. Hoyland, M. Hueller, H. Inchauspé, O. Jennrich, P. Jetzer, N. Karnesis, B. Kaune, N. Korsakova, C. J. Killow, J. A. Lobo, I. Lloro, L. Liu, J. P. López-Zaragoza, R. Maarschalkerweerd, D. Mance, N. Meshksar, V. Martín, L. Martin-Polo, J. Martino, F. Martin-Porqueras, I. Mateos, P. W. McNamara, J. Mendes, L. Mendes, M. Nofrarias, S. Paczkowski, M. Perreur-Lloyd, A. Petiteau, P. Pivato, E. Plagnol, J. Ramos-Castro, J. Reiche, D. I. Robertson, F. Rivas, G. Russano, J. Slutsky, C. F. Sopena, T. Sumner, D. Texier, J. I. Thorpe, D. Vetrugno, S. Vitale, G. Wanner, H. Ward, P. Wass, W. J. Weber, L. Wissel, A. Wittchen, and P. Zweifel, *Phys. Rev. D* **97**, 122002 (2018).
- [22] C. Trenkel, *Prediction of spacecraft magnetic field*, Tech. Rep. S2-ASU-TN-2523 (Airbus, 2015).
- [23] S. Vitale, *Effect of Eddy currents on down-conversion of magnetic noise.*, Tech. Rep. Memo LTP package (University of Trento, 2007).
- [24] L. Trounau, *AC magnetic susceptibility of LPF TMs, issue 2*, Tech. Rep. TEC-EEE/2007149/LT (ESA, 2007).
- [25] L. Trounau, *Impact of LTP thermal diagnostics on magnetic acceleration noise budget*, Tech. Rep. S2-EST-TN-2026 (ESA, 2008).
- [26] H. Fang, *Magnetic susceptibility (d.c.) measurement of FM Test Mass 4 submitted for test by CGS S.p.A.*, Tech. Rep. (Bureau International des Poids et Mesures, 2012).
- [12] M. Armano, H. Audley, J. Baird, P. Binetruy, M. Born, D. Bortoluzzi, E. Castelli, A. Cavalleri, A. Cesarini, A. M. Cruise, *et al.*, *Astroparticle Physics* **98**, 28 (2018).
- [13] M. Armano *et al.*, *Phys. Rev. Lett.*
- [14] L. Néel, *Annales de Géophysique* **5**, 99 (1949).
- [15] H.-U. Worm, D. Clark, and M. J. Dekkers, *Geophysical Journal International* **114**, 127 (1993).
- [16] M. Jackson, B. Moskowicz, J. Rosenbaum, and C. Kissel, *Earth and Planetary Science Letters* **157**, 129 (1998).
- [17] F. Hrouda, J. Pokorný, J. Ježek, and M. Chadima, *Geophysical Journal International* **194**, 170 (2013).
- [18] J. Ježek and F. Hrouda, *Physics of the Earth and Planetary Interiors* **274**, 138 (2018).
- [19] M. Jackson, *The IRM Quarterly* **13**, 10 (2003).
- [20] M. Armano, H. Audley, G. Auger, J. T. Baird, M. Bassan, P. Binetruy, M. Born, D. Bortoluzzi, N. Brandt, M. Caleno, L. Carbone, A. Cavalleri, A. Cesarini, G. Ciani, G. Congedo, A. M. Cruise, K. Danzmann, M. de Deus Silva, R. De Rosa, M. Diaz-Aguiló, L. Di Fiore, I. Diepholz, G. Dixon, R. Dolesi, N. Dunbar, L. Ferraioli, V. Ferroni, W. Fichter, E. D. Fitzsimons, R. Flatscher, M. Freschi, A. F. García Marín, C. García Marirrodiga, R. Gerndt, L. Gesa, F. Gibert, D. Giardini, R. Giusteri, F. Guzmán, A. Grado, C. Grimaldi, A. Grynagier, J. Grzysch, I. Harri-